Am J Physiol Cell Physiol 325: C1470–C1484, 2023.
First published October 30, 2023; doi:10.1152/ajpcell.00200.2023

american physiological society

AMERICAN JOURNAL OF PHYSIOLOGY
CELL PHYSIOLOGY

RESEARCH ARTICLE

A biologically validated mathematical model for decoding epithelial apical, basolateral, and paracellular electrical properties

Colby F. Lewallen,[1] Athena Chien,[2] Arvydas Maminishkis,[3] Rishabh Hirday,[1] Dominik Reichert,[1] Ruchi Sharma,[1] Qin Wan,[1] Kapil Bharti,[1]* and Craig R. Forest[2,4]*

[1]*Ocular and Stem Cell Translational Research Section, Ophthalmic Genetics and Visual Function Branch, National Eye Institute, Bethesda, Maryland, United States;* [2]*Wallace H. Coulter Department of Biomedical Engineering, Georgia Institute of Technology, Atlanta, Georgia, United States;* [3]*Translational Research CORE, Ophthalmic Genetics and Visual Function Branch, National Eye Institute, Bethesda, Maryland, United States; and* [4]*G.W. Woodruff School of Mechanical Engineering, Georgia Institute of Technology, Atlanta, Georgia, United States*

Abstract

Epithelial tissues form selective barriers to ions, nutrients, waste products, and infectious agents throughout the body. Damage to these barriers is associated with conditions such as celiac disease, cystic fibrosis, diabetes, and age-related macular degeneration. Conventional electrophysiology measurements like transepithelial resistance can quantify epithelial tissue maturity and barrier integrity but are limited in differentiating between apical, basolateral, and paracellular transport pathways. To overcome this limitation, a combination of mathematical modeling, stem cell biology, and cell physiology led to the development of 3 P-EIS, a novel mathematical model and measurement technique. 3 P-EIS employs an intracellular pipette and extracellular electrochemical impedance spectroscopy to accurately measure membrane-specific properties of epithelia, without the constraints of prior models. 3 P-EIS was validated using electronic circuit models of epithelia with known resistances and capacitances, confirming a median error of 19% (interquartile range: 14%–26%) for paracellular and transcellular resistances and capacitances ($n = 5$). Patient stem cell-derived retinal pigment epithelium tissues were measured using 3 P-EIS, successfully isolating the cellular responses to adenosine triphosphate. 3 P-EIS enhances quality control in epithelial cell therapies and has extensive applicability in drug testing and disease modeling, marking a significant advance in epithelial physiology.

NEW & NOTEWORTHY This interdisciplinary paper integrates mathematics, biology, and physiology to measure epithelial tissue's apical, basolateral, and paracellular transport pathways. A key advancement is the inclusion of intracellular voltage recordings using a sharp pipette, enabling precise quantification of relative impedance changes between apical and basolateral membranes. This enhanced electrochemical impedance spectroscopy technique offers insights into epithelial transport dynamics, advancing disease understanding, drug interactions, and cell therapies. Its broad applicability contributes significantly to epithelial physiology research.

electrophysiology; epithelial tissues; epithelial transport dynamics; mathematical model; retinal pigment epithelium

INTRODUCTION

Epithelial cells form a barrier that plays a crucial role in the selective transport of ions, nutrients, and waste products throughout the body (1–3). Damage or degeneration of these barrier-type tissues is often associated with common pathological conditions, such as celiac disease (4), cystic fibrosis (5), diabetes (6), and age-related macular degeneration (7), which collectively impact millions of people worldwide (8–12). Various techniques are used to study the pathologies of these diseases in epithelial tissues, including morphology (13), protein biomarkers (14), gene expression (15), and electrophysiology (7). Among these techniques, electrophysiology stands out as one of the few techniques that can provide insight into epithelial barrier function by measuring the electrical properties associated with the transport of critical ions, nutrients, and waste products in an environment similar to in vivo conditions (7, 16). The most common measurement of epithelial electrophysiology is transepithelial resistance (TER), which is generally used to assess the formation of a barrier between epithelial cells by the tight junctions (7, 17–27). Additionally, some groups use electrochemical impedance spectroscopy (EIS) to quantify the transepithelial capacitance (TEC), which is parallel to the TER (see Fig. 1*B*) and may be proportional to morphological characteristics such as microvilli formation and basolateral infoldings (23, 27). The TER and TEC are

*K. Bharti and C. R. Forest contributed equally to this work.
Correspondence: C. R. Forest (cforest@gatech.edu).
Submitted 11 May 2023 / Revised 26 October 2023 / Accepted 26 October 2023

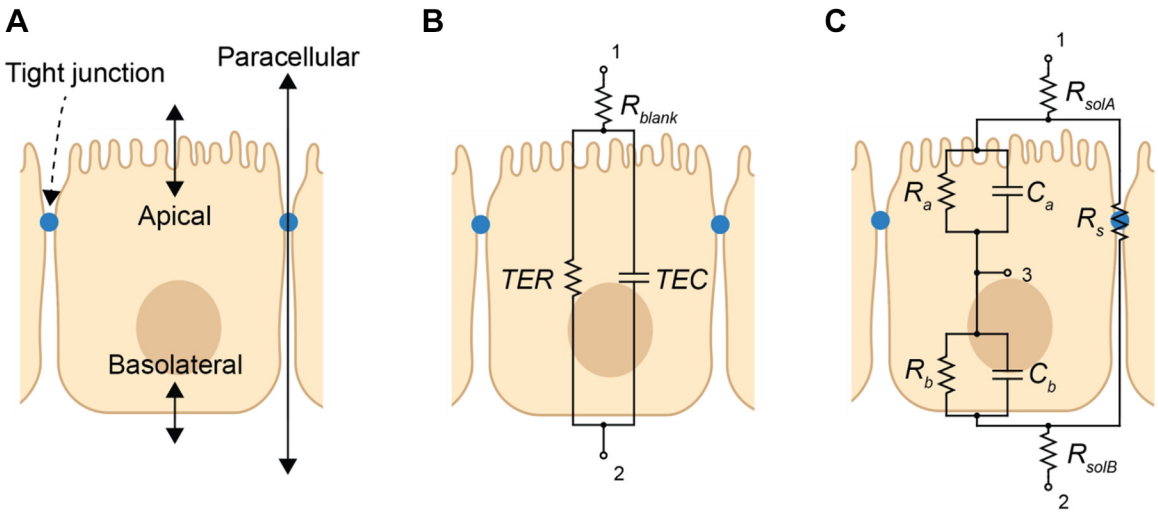

Figure 1. Schematics of ion transport in epithelia. *A*: physical model: cross-section schematic of an epithelial tissue showing the 3 pathways where transport is regulated. *B*: extracellular circuit model: A simple resistor-capacitor (RC) circuit model used to represent the net transport of charge across an epithelial tissue. Specifically, the combined resistance to ion flow from the apical, basolateral, and paracellular (shunt) pathways is called the transepithelial resistance (TER), and the net flow of charge via capacitive pathways (e.g., across the plasma membranes) is called transepithelial capacitance (TEC). These parameters are widely utilized in the field despite their low fidelity and because they can be readily measured with commercial instrumentation. The resistance of the surrounding media and growth substrate is represented by a series resistor R_{blank}. *C*: intracellular circuit model: a circuit model of ion transport that considers separate equivalent electrical properties of the apical, basolateral, and paracellular (shunt) pathways as follows: R_s, shunt pathway resistance; R_a and C_a, apical resistance and capacitance; R_b and C_b, basolateral resistance and capacitance (32). The resistance of the surrounding media and growth substrates are represented by 2 additional, series resistors R_{solA} and R_{solB} for the apical and basolateral sides of the epithelial tissue, respectively. Created with BioRender.com.

typically measured in commercially available devices such as an Ussing chamber (28), EndOhm (29), or STX2 (29) by placing electrodes on either side of the tissue layer at *nodes 1* and *2* in Fig. 1*B* and measuring the electrical response of the tissue to a stimulus (30–32).

These transepithelial measurements combine the apical, basolateral, and shunt (paracellular) transport pathways of epithelial tissues (Fig. 1*A*) into a single resistor or a simple parallel resistor and capacitor circuit (25, 33–35).[1] However, each pathway can have unique permeabilities to ions, making it necessary to independently characterize the electrical properties of each pathway using the intracellular circuit model in Fig. 1*C*, especially in disease, drug, and transport studies (30–32, 38–42).

Traditional electrophysiological methods, which often use a single sharp pipette inserted into the cell as illustrated in *node 3* of Fig. 1*C*, enable continuous measurements of apical or basolateral membrane voltages. These voltages can then be leveraged to estimate relative changes between the apical and basolateral transport pathways (38, 39). However, these traditional approaches still cannot measure the resistances or capacitances of apical, basolateral, and shunt pathways without relying on additional assumptions. These assumptions might include that the shunt resistance (R_s) remains constant, is practically infinite, or maintains a fixed ratio with the sum of the cell membrane resistances ($R_a + R_b$) (29, 41–45). Such assumptions can obscure the underlying mechanisms, be they isolated increases in apical channel permeability, a combined effect involving both apical and basolateral channels, or changes restricted to basolateral channels, making it challenging to decipher the exact alterations in epithelial transport pathways.

This paper presents a mathematical model and measurement technique, called 3 P-EIS, to obtain the membrane specific properties of intact epithelial tissues as shown in Fig. 1*C*, without the need for additional measurement hardware (e.g., additional pipettes), underlying assumptions, or constraints based on cell morphology, physiology state, or function. 3 P-EIS was validated using an electric circuit board model of intact epithelia and tested biologically using an induced pluripotent stem cell (iPSC)-derived retinal pigment epithelial (RPE) tissue to quantify the well-known response of this tissue to the apical application of adenosine triphosphate (ATP) (38, 39). This technique can provide unique insights into the functional state of the apical and basolateral membranes of intact epithelia, as well as separate the contributions of the paracellular pathway from the TER. Thus it enables a more comprehensive understanding of the mechanisms underlying various diseases, drug responses, and environmental stimuli, without previous, restrictive assumptions about cell processes.

[1]The term "basolateral" in Fig. 1*A* refers to the apparent (i.e., measured) impedance of the combination of the true basal and lateral cell membrane impedances. Furthermore, the "shunt" resistance encapsulates paracellular transport pathway resistances and any experimental artifacts like electrical current leak through the boundary between the Ussing chamber and epithelial cell layer. Paracellular pathways in epithelial cells usually involve both tight junctions and the lateral intercellular space (LIS), connected in series. Without inserting an additional, intermediate pipette into the LIS, by using multiple intracellular pipettes, or by making assumptions about membrane properties, it is not possible to distinguish between the resistances of the tight junction and the LIS (36). Therefore, Fig. 1*C* lumps all nontranscellular transport pathways into a single shunt resistor. For an in-depth derivation of the circuit model in Fig. 1*C*, consult Refs. 36, 37.

MATERIALS AND METHODS

Data Acquisition

Electrode configuration.

The apical and basolateral bath voltages (V_a and V_b, respectively) were measured to determine the transepithelial potential (TEP). These voltages were recorded using Ringer-filled 3.5% agar bridges connected to saturated KCl baths with submerged, double-junction AgCl reference electrodes (Fisher Scientific, Accumet, cat. no. 13-620-855). The TEP was amplified using a VCC 600 (Physiologic Instruments) with inputs V_1 and I_1 connected to the apical bath, and inputs V_2 and I_2 connected to the basolateral bath (*nodes 1* and *2* in Fig. 1*C*, respectively). The VCC 600 function mode was set to "OPEN," the fluid resistance compensation was set to 0, and the offset toggle was set to the "OFF" position.

The PGSTAT204 reference electrode was connected to the basolateral bath (*node 2* in Fig. 1*C*), and the sense electrode was connected to the apical bath (*node 1* in Fig. 1*C*) through the same Ringer-based agar bridges used to record the TEP, preamplification. However, the counter electrode was connected to a 0.01-in. diameter Ag|AgCl wire, directly submerged in the basolateral bath and the working electrode was connected to an identical Ag|AgCl wire, directly submerged in the apical bath.

The protocol for inserting a pipette in the cell's cytoplasm (*node 3* in Fig. 1*C*) for intracellular voltage recordings was described previously (46), which in turn builds upon prior work in automated intracellular electrophysiology (47–50). Briefly, a LabVIEW algorithm was used to insert a pipette into the cytoplasm of a single cell using a N-565.260 piezoelectric motor connected to a E-861.1A1 single-axis controller box (Physik Instrumente). The pipette voltage (V_p) was amplified using a Multiclamp 700B (Molecular Devices) amplifier in "IC" mode. The primary output of the Multiclamp 700B had the following settings: 10 mV/mV in "Membrane Potential" mode with "gain" set to 1, and the Bessel filter was set to 30 kHz.

Recording hardware.

The TEP and pipette voltages were continuously recorded during each experiment at sampling rate of 20.1 kHz using a NI USB-6356 DAQ, where $TEP(t) = V_1(t) - V_2(t)$ and $V_p(t) = V_1(t) - V_3(t)$, where the numerical subscripts correspond to voltages recorded at *nodes 1*, *2*, and *3* in Fig. 1*C* as a function of time, t. In this hardware configuration, the apical solution and apical membrane potential are measured directly by the pipette; thus $V_a = V_p$. Consequently, the basolateral solution and basolateral membrane potential are calculated using $V_b(t) = V_2(t) - V_3(t) = -\big(TEP(t) - V_a(t)\big)$.

Electrochemical impedance spectroscopy.

Galvanostatic EIS measurements were performed with an Autolab PGSTAT204 with a FRA32M integrator module (Metrohm AG) connected to *nodes 1* and *2* in Fig. 1*C*. NOVA 2.1.5 software was used to perform frequency sweeps from 0.5 Hz to 10 kHz with ATOP = 4 μA using the "5 sines" wave type setting, spaced at five measurements per decade. This resulted in an ~2-min measurement with 106 unique frequencies, logarithmically spaced.

Model Assessment

Electronic cell.

An electric circuit was constructed on a breadboard, with equivalent resistor and capacitor components arranged to match the cell circuit diagram in Fig. 1*C* These equivalent cell models were created with all possible permutations of the following:

- C_a, C_b = [0.1 μF, 1 μF, 2.2 μF];
- R_a, R_b, R_s [100 Ω, 1 kΩ, 10 kΩ]; and
- R_{solA}, R_{solB} [0 Ω, 100 Ω]

These values were selected to represent the range of previously reported membrane properties of epithelia while keeping the experimental permutations reasonable (31, 36, 43, 44, 51–53). The actual resistance and capacitance values of the physical circuit elements, however, were also measured with a digital multimeter (FLUKE 287). The validated resistances and capacitances for each parameter are shown in the Supplemental Material. This resulted in $3 \times 3 \times 3 \times 3 \times 3 \times 2 \times 2 = 972$ possible permutations. This electronic cell model was used to simulate recordings from biological cells. Therefore, the measuring probes for the PGSTAT and Thompson clamp were directly connected to the equivalent apical bath, basolateral bath, and cell cytoplasm (*nodes 1*, *2*, and *3* in Fig. 1*C*, respectively).

Additional circuit models.

Classically, intracellular electrophysiology data are analyzed using a term called the voltage divider ratio (VDR). VDR represents the approximate ratio between the apical and basolateral membrane resistances. The VDR overcomes the limitation of traditional intracellular electrophysiology setups that cannot separately monitor transcellular and shunt current. Without a direct, simultaneous measurement of both voltage and current through the cytoplasm of the cell using the intracellular electrode, it is impossible to solve for the apical, basolateral, and shunt resistances using Ohm's law.

To calculate the VDR, the voltage change generated by an extracellular, alternating current is applied at very low frequencies (e.g., $f \leq 0.5$ Hz). Furthermore, the VDR assumes the apical and basolateral membrane currents (i_a and i_b, respectively) to be identical and the surrounding solution and background resistances R_{solA} and R_{solB} to be negligible relative to R_a and R_b. Consequently, by measuring the magnitude of the voltage change across the apical and basolateral membranes, the VDR provides an approximation for the ratio of the apical to basolateral membrane resistances (25, 31):

$$VDR\left(\omega = \pi\frac{\text{rad}}{\text{s}}\right) = \frac{|V_a(\omega)|/|i_a(\omega)|}{|V_b(\omega)|/|i_b(\omega)|} \cong \frac{R_a}{R_b}. \quad (1)$$

Extracellular electrophysiology parameters, as shown in Fig. 1*B*, are often reported as a single, transepithelial resistance (TER), which is calculated using Ohm's law, $V = IR$, where V is the potential difference, I is the electric current, and R is the electrical resistance, at similarly low frequencies ($f \leq 0.5$ Hz). Consequently, traditional TER is measured as

$$TER\left(\omega = \pi\frac{\text{rad}}{\text{s}}\right) = \frac{|TEP(\omega)|}{|i_{applied}(\omega)|} = R_{solA} + R_{solB} + \frac{R_s(R_a + R_b)}{R_s + R_a + R_b}, \quad (2)$$

where $|i_{applied}|$ is the magnitude of the applied current.

In this paper, the TER and VDR are computed, serving as the current gold standard for electrophysiological assessment of epithelial tissues. The data obtained using these traditional measures are denoted as "3 P-Classical." In contrast, when utilizing the novel technique introduced in this paper for the calculation of the membrane-specific parameters R_a, R_b, R_s, C_a, and C_b from Fig. 1*C*), the model is referred to as "3 P-EIS."

Additionally, to investigate the necessity of incorporating intracellular voltage data for the accurate calculation of membrane-specific electrical parameters, a variant of the 3 P-EIS model was implemented, hereafter referred to as the 2 P-EIS model. In the 2 P-EIS model, the extracellular EIS data, both real impedance and imaginary impedance, were fit to the circuit model identical to the 3 P-EIS model. In other words, the intracellular data corresponding to *node 3* in Fig. 1*C* were deliberately excluded in the 2 P-EIS analysis. This comparative approach served dual purposes: *1*) to assess the predictive capacity of the model in the absence of intracellular data by observing any parameter (β_k) variability; and *2*) to quantitatively evaluate the improvements in fit accuracy uniquely attributable to the inclusion of intracellular data in the 3 P-EIS model.

Electrophysiology

Human iPSC-RPE cells.

The protocol for induced pluripotent stem cell (iPSC) differentiation has been described previously (54). Briefly, for each iPSC-derived sample, somatic cells were isolated from a single donor and were reprogrammed using Sendai virus reprogramming methods and then differentiated into iPSC-derived RPE (54). iPSC-derived RPE cells were seeded on Corning 3460 Transwells, with a seeding density of 250,000 cells/cm^2. Two human donors were used to derive iPSC-RPE for this experiment. *Samples 1* and *2* were derived from *donor A* and *sample 3* was derived from *donor B*. Human materials and cells were handled according to institutional review board-approved protocol 11-EI-0245.

Pipette fabrication.

Sharp microelectrode pipettes were pulled from fire-polished borosilicate glass with a filament (Sutter Instrument, no. BF100-50-10, 1-mm outer and 0.5-mm inner diameter) on a P-97 puller with a 2.5 × 2.5 mm box filament (Sutter Instrument). The pipettes were pulled in a single cycle (~10 s) such that the resulting pipette had a tip size 100–200 nm in diameter (validated with scanning electron microscopy) and corresponding resistance of 120–250 MΩ when filled with 150 mM KCl. Pipettes with junction potential magnitudes larger than 12 mV were discarded.

Tissue mounting and maintenance.

The method for mounting the tissue into the modified Ussing chamber for electrophysiology has been described previously (46). In short, a 7-mm diameter circular section of the iPSC-RPE Transwell membrane was punched out, mounted, and sealed into the chamber, apical side up. Electrical current leak, due to poor sealing between the Ussing chamber and the Transwell punch-out, was minimized by placing a nylon mesh insert beneath the sample so that the iPSC-RPE made contact around the entire circumference of the chamber, as described previously (46). The total exposed tissue cross section was ~0.11 cm^2. Experimental solutions were perfused across both sides of the tissue for the entire duration of the experiment.

Perfusion rates across the apical and basolateral sides of the tissue were gravity driven using fixed-height manifolds at ~4.5 mL/min and were manually adjusted using a threaded tube clamp. The Ussing chamber was coated in a hydrophobic solution (Sigmacote, Sigma-Aldrich) and perfusion solution tubing was heated with a custom water jacket so that the temperature of the solution perfusing across the tissue was ~36°C (SD 0.5). The waste solutions of the apical and basolateral baths were kept electrically isolated using two different flasks.

Electrophysiological solution.

The standard control solution, modified Ringer's solution, is the same as described in Lewallen et al (46). In brief, the solution contains (in mM): 5 KCl, 116.5 NaCl, 23 $NaHCO_3$, 0.5 $MgCl_2$, 1.8 $CaCl_2$, 2 taurine, 5 glucose, and 10 sucrose. All salts (except for $CaCl_2$) were mixed into de-ionized water at room temperature (20°C). The solution was bubbled for ~5 min with 95% CO_2 before the addition of $CaCl_2$. After all salts were dissolved into the Ringer's solution, the solution had an osmolality of 295 mosmol/kgH_2O (SD 5). During each experiment, the solution was continuously bubbled with a custom gas mixture (8% CO_2, 10% O_2, and 82% N_2) to maintain the Ringer's solution pH near 7.4 (SD 0.1) near the cells inside the Ussing chamber (46, 55, 56).

Experimental protocol.

The tissue was mounted in the Ussing chamber at an angle ~30° from horizontal. After successfully inserting the pipette into a cell cytoplasm, the tissue was given 30 min to reach steady state (i.e., baseline). Then, for ~10 min, 100 μM of fresh ATP was dissolved into Ringer's solution perfusing the apical side of the RPE to induce well-established electrophysiological changes (38, 39). Finally, the apical Ringer's solution was switched back to the previously described Ringer's formulation for an additional 30 min.

The combined EIS and intracellular electrophysiology methods were performed on RPE cells, studying the ATP response as a function of time. Using the methods previously described, the unique resistance and capacitance values in these cells were calculated at each time point. Specifically, for a typical 1-h experiment, with each measurement taking ~2 min, ~30 time points were obtained for each of the apical, basolateral, and shunt properties.

Signal Processing

Data fitting.

For brevity, the circuit parameters illustrated in Fig. 1*C*, namely R_a, R_b, C_a, C_b, R_s, R_{solA}, and R_{solB}, are represented by the term β_k, where k represents a specific circuit parameter (e.g., $\beta_k = R_a$). To calculate all β_k, the circuit model was fit to

the measured data using Matlab's nonlinear least squares solver, 'lsqcurvefit,' with the settings described in Table 1.

The circuit parameter limits were set as follows:

- $C_a, C_b \in [1 \times 10^{-5}\ \mu F, 1 \times 10^{2}\ \mu F]$;
- $R_a, R_b, R_s \in [1\ \Omega, 5 \times 10^{5}\ k\Omega]$; and
- $R_{solA}, R_{solB} \in [1 \times 10^{-2}\ \Omega, 250\ \Omega]$.

To mitigate the risk of converging to local minima or boundary values, each fitting procedure was initialized 500 times with randomized starting values. The bounds and starting points were chosen to span the ranges of previously reported membrane properties in epithelial tissues (31, 36, 43, 44, 51).

Data normalization.

There were two different normalizations performed during each fit: *1*) the magnitude of each circuit element, β_k, was converted to a log10 domain, and (2) the real impedance, imaginary impedance, and membrane ratio were normalized to their respective maximum values.

Specifically, the resistors and capacitor circuit elements had vastly different orders of magnitude and needed to be adjusted so that the fitting algorithm assigned equal "weight" to the relative error of each parameter. (see *Data fitting*). Therefore, to ensure that the magnitude of each parameter was roughly equal, the model parameters in Fig. 1*C*, β_k, were converted to a log-base 10 system: $\hat{\beta}_k = \log_{10}(\beta_k)$. Later, inside the custom fitting function, we converted the fitted parameter $\hat{\beta'}_k$ back to the original, non-log-base 10 values, $\beta'_k = 10^{\beta'_k}$.

Following similar logic, the real impedance, imaginary impedance, and membrane ratio could also span vastly different ranges. Thus, to ensure the sum of the relative error magnitudes for each input vector, D, was approximately equal, they were preprocessed by dividing by the maximum magnitude such that the real impedance, imaginary impedance, and membrane ratio all spanned the range of [−1, 1]. Specifically,

$$\hat{D} = \frac{D}{\max_{d \in D} |d|}. \tag{3}$$

Consequently, the value for the fit real impedance, imaginary impedance, and membrane ratio magnitudes and residuals (r) had to be multiplied by the maximum values that were extracted in the preprocessing phase to return the correct magnitude. Specifically,

$$D' = \hat{D}' \max_{d \in D} |d| \tag{4}$$

and

$$r = \hat{r} \max_{d \in D} |d|. \tag{5}$$

Fourier transform.

The magnitudes of both membrane potentials as a function of frequency [$|V_a(\omega)|$ and $|V_b(\omega)|$] were computed from $V_a(t)$ and $V_b(t)$ using the short-time Fourier transform (STFT) function (stft, Matlab, Mathworks, Natick, MA). This was done by taking the Fourier transforms of small Hanning windowed segments of $V_a(t)$ and $V_b(t)$.

The STFT numerical method is preferred over the fast Fourier transform (FFT) in this application: due to abrupt changes in frequency inherent to the EIS measurement technique, there are discontinuities in the time domain, which lead to spectral leakage when using a conventional FFT algorithm. The following STFT input arguments and definitions were used in the Matlab algorithms developed for this work to calculate the amplitude of V_a and V_b at each of the frequencies:

- Signal_fraction: samples in the signal that contain frequency ω_n divided by total number of samples in the signal.
- Window_length: 80% of the signal_fraction; and
- Window: the Hanning window function was used to evaluate the subset of the signal that contains the frequency ω_n, with an overlap length of 75% of the window_length.

Analysis of a measurement was repeated for each frequency. Low frequencies (e.g., 0.5 Hz) required a much longer time to get a minimum of three cycles per frequency than higher frequencies (e.g., 10 kHz). Using a single window size for all frequencies increased measurement error significantly. Window sizes approximately equal to the signal fraction of high frequencies had large errors in the measured low-frequency amplitude likely due to insufficient cycles inside the window. Large errors in high frequencies were observed with larger window sizes (≅ to signal fraction of low frequencies) that exceeded the duration of the applied high-frequency signal. Signals that start and end within a single window have reduced power in an FFT calculation and need to be corrected by dividing by the signal fraction (as discussed above). Due to the limitations of the EIS hardware and software, the exact

Table 1. *Equations and parameter values*

Parameter	Value	Description
Algorithm	'trust-region-reflective'	Optimization algorithm used
MaxIterations	1×10^4	Maximum number of iterations allowed
MaxFunctionEvaluations	1×10^4	Maximum number of function evaluations allowed
FunctionTolerance	K_e * norm($f' - f_{measured}$)	Tolerance for convergence based on the function value
OptimalityTolerance	K_e * norm($f' - f_{measured}$)	Tolerance for convergence based on the gradient of the function
FiniteDifferenceStepSize	$max\left(eps^{\frac{1}{3}}, min\left(1e-4, K_e * norm(f' - f_{measured})\right)\right)$	Step size for approximating the Jacobian matrix
TypicalX	$K_e . * \left[R'_a, R'_b, C'_a, C'_b, R'_s, R'_{solA}, R'_{solB}\right]'$	Scaling factors for the parameters during optimization

This table enumerates the specific equations and parameter values β′ configured for matlab's 'optimoptions' function, which were subsequently applied to the 'lsqcurvefit' algorithm for curve fitting. The settings detailed in this table are the nondefault options utilized in this paper and were selected based on guidelines provided in matlab's SimBiology documentation pertinent to biological data fitting. See GLOSSARY for definitions.

duration of any frequency was not known. Therefore, the duration of each frequency was estimated using the start time of each frequency; a value reported by the EIS software. A representative STFT result is shown in the Supplemental Material.

From the STFT, the amplitude $|V(\omega)|$ at each frequency needed to be extracted. At each frequency, the STFT was cropped to a time region of interest (ROI). As discussed above, defining the time ROI required overcoming inherent limitations in the NOVA software. Specifically, the time ROI was set to begin 2 s before the reported initiation time of the applied frequency by the EIS software. Similarly, the time ROI was set to end 2 s after the start of the next applied frequency.

After cropping the STFT of the time domain data, the data was then cropped at the target frequency. This generated a time and frequency ROI that contained a subset of the calculated signal amplitudes. The maximum amplitude, or *stft_amp*, was extracted from this ROI. This maximum value was converted to amplitude as in

$$|V(\omega)| = 4\left|\frac{stft\_amp}{window\_length}\right|. \tag{6}$$

Evaluation metrics for fitting and parameter accuracy. To thoroughly assess the efficacy of the mathematical model and fitting algorithm, two distinct yet complementary avenues of error quantification were deployed. The first, referred to as residual error, gauges the ability of the model to fit the measured data at all measured frequencies (ω). This was quantified using the equation

$$r(\omega) = |d'(\omega) - d(\omega)|. \tag{7}$$

In this equation, $r(\omega)$ is the residual error at a given frequency, and $d'(\omega)$ and $d(\omega)$ are the model-predicted and actual measurements, respectively, for either the real impedance, imaginary impedance, or membrane ratio.

The second metric, parameter estimation error, is encapsulated by the equation

$$\varepsilon_k = \frac{|\beta_k' - \beta_k|}{\beta_k} \times 100. \tag{8}$$

In this instance, β_k' is the estimate derived from the fitting algorithm, while β_k is the independently measured value obtained via a multimeter. The parameter estimation error was performed on both the 2 P-EIS and 3 P-EIS models and is a percentage.

These dual metrics offer a comprehensive view of model performance. Large residual errors may signal a suboptimal model choice, while significant parameter estimation errors would suggest inaccurate circuit element representation in the model.

RESULTS AND DISCUSSION

Mathematical Model for Experimental Fit

This paper utilizes a mathematical model of the circuit in Fig. 1*C* to quantify the electrical properties of epithelia. The transepithelial model of impedance is complex and can be represented as the sum of two orthogonal vectors: the real impedance, $X(\omega)$, and the imaginary impedance, $Y(\omega)$. This representation is based on the mathematical concept of complex numbers, where the complex impedance, $Z_{abs}(\omega)$, can be expressed as

$$Z_{abs}(\omega) = X(\omega) + jY(\omega), \tag{9}$$

where j represents the imaginary unit ($\sqrt{-1}$). This representation allows for separate measurements and analysis of the real and imaginary components of the impedance, which is a powerful tool in characterizing the electrical properties of the epithelial tissue. Additionally, the measured complex impedance, Z_{abs}, in *Eq. 9* can be mathematically modeled by combining the circuit elements in Fig. 1*C* such that

$$Z'_{abs}(\omega) = R_{solA} + R_{solB} + \frac{R_s(Z_a(\omega) + Z_b(\omega))}{R_s + Z_a(\omega) + Z_b(\omega)} \tag{10}$$

where

$$Z_a(\omega) = \frac{R_a}{1 + j\omega R_a C_a} \tag{11}$$

and

$$Z_b(\omega) = \frac{R_b}{1 + j\omega R_b C_b}. \tag{12}$$

Note that, as in *Eq. 9*, Z'_{abs} is complex and can be rewritten in a similar form

$$Z'_{abs}(\omega) = X'(\omega) + jY'(\omega), \tag{13}$$

where

$$X'(\omega) = R_{solA} + R_{solB} + \frac{R_s(R_a + R_b)\left(R_a + R_b + R_s - C_a C_b R_a R_b R_s \omega^2\right)}{\sigma 1} + \frac{R_s\left(C_a R_a R_b \omega + C_b R_a R_b \omega\right)\left(C_a R_a R_b \omega + C_b R_a R_b \omega + C_a R_a R_s \omega + C_b R_b R_s \omega\right)}{\sigma_1} \tag{14}$$

and

$$Y'(\omega) = \frac{R_s\left(C_a R_a R_b \omega + C_b R_a R_b \omega\right)\left(R_a + R_b + R_s - C_a C_b R_a R_b R_s \omega^2\right)}{\sigma_1} - \frac{R_s(R_a + R_b)\left(C_a R_a R_b \omega + C_b R_a R_b \omega + C_a R_a R_s \omega + C_b R_b R_s \omega\right)}{\sigma_1} \tag{15}$$

with

$$\sigma_1 = \left(R_a + R_b + R_s - C_a C_b R_a R_b R_s \omega^2\right)^2 + \left(C_a R_a R_b \omega + C_b R_a R_b \omega + C_a R_a R_s \omega + C_b R_b R_s \omega\right)^2. \quad (16)$$

In addition to Z_{abs}, this paper describes a new, independent parameter: the membrane ratio $\alpha(\omega)$. The membrane ratio is an extension of the VDR (*Eq. 1*), measured at many frequencies, rather than a single, low frequency. Thus, the membrane ratio is similarly defined as

$$\alpha(\omega) = \frac{|V_a(\omega)|}{|V_b(\omega)|}. \quad (17)$$

Because the membrane ratio is a ratio of magnitudes, it is not a complex number and has no units. The mathematical model of the membrane ratio (α') can be derived as a function of the circuit parameters in Fig. 1*C* such that

$$\alpha'(\omega) = \frac{Z_a(\omega)R_s + R_{solA}(Z_a(\omega) + Z_b(\omega) + R_s)}{Z_b(\omega)R_s + R_{solB}(Z_b(\omega) + Z_b(\omega) + R_s)}, \quad (18)$$

Note that when ω is very low (e.g., 0.5 Hz), and when R_{solA} and R_{solB} are both much lower than R_a and R_b, that $\alpha \cong$ VDR. Recall that each circuit element in Fig. 1*C* can be treated as an element in an array, β_k, where the subscript k represents the kth element in the array (e.g., $\beta_1 = R_{solA}$, $\beta_2 = R_a$, etc.). The measured values for the real impedance $X(\omega)$, the imaginary impedance $Y(\omega)$, and the membrane ratio $\alpha(\omega)$ can be modeled by a unique combination of β_k to calculate $X'(\omega)$, $Y'(\omega)$, and $\alpha'(\omega)$ from *Eqs. 14*, *15*, and *18*. Therefore, as described in MATERIALS AND METHODS, the electrical properties of a monolayer can be determined by using a nonlinear least squared solver to minimize an objective function, J, which is defined as the sum of the squared residuals, or error, between the measured and modeled data at all frequencies. In mathematical form, J is calculated as

$$J = \sum_{i=1}^{n}\Big(\left(X(\omega_i) - X'(\omega_i)\right)^2 + \left(Y(\omega_i) - Y'(\omega_i)\right)^2 + \left(\alpha(\omega_i) - \alpha'(\omega_i)\right)^2\Big) \quad (19)$$

where i represents each discrete frequency, ω, out of n total frequencies. The values for β_k that minimize the error are defined as the fit values, β_k'.

The mathematical model described above represents a significant advancement in the field of epithelial transport electrophysiology. Unlike previous intracellular electrophysiology methods, this model enables measurements of the apical, basolateral, and shunt electrical transport properties without relying on potentially incorrect assumptions (e.g., the shunt resistance is fixed or a constant percentage of TER) (41, 44, 57). By eliminating the need for time-consuming and resource-intensive follow-up experiments to validate how each pathway is separately affected in an experiment, this model can significantly increase the efficiency and accuracy of drug discovery and disease research.

Parameter Fitting on Electronic Cell Model

Representative examples of impedance data.

Figure 2 can be visually inspected to qualitatively evaluate the electrical properties of an epithelial tissue. For example,

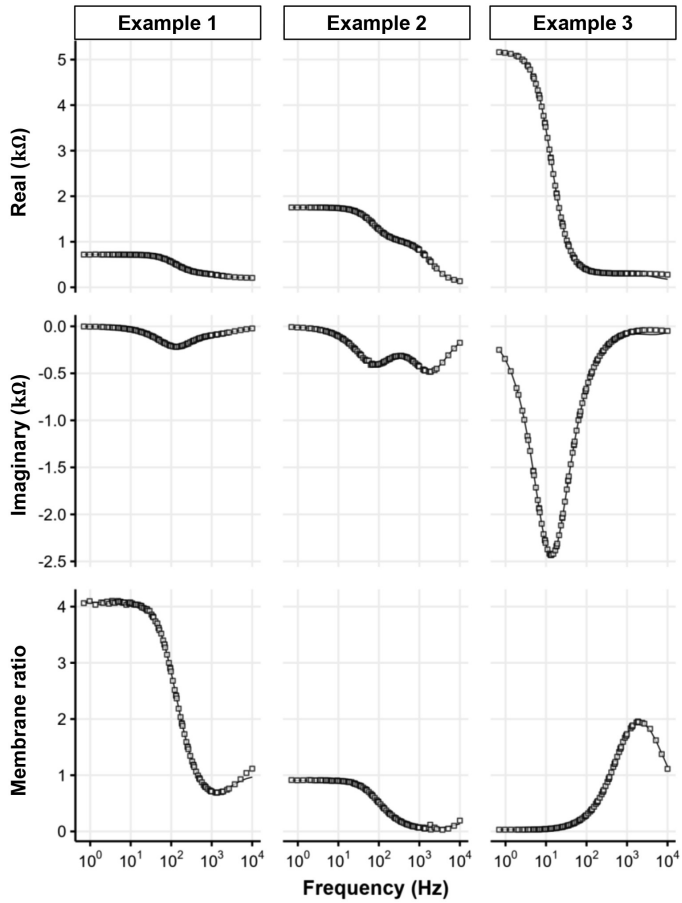

Figure 2. Selected examples of both measured and fitted data from 3 distinct electronic model circuits, indicating the correlation of the 3 P-EIS model with the measured impedance data. The data is organized in columns, with each column corresponding to 1 of 3 example circuits that emulate low-, medium-, and high-transepithelial resistance epithelial tissues. Each column is divided into 3 rows, where the *top row* illustrates measured, real impedance values [$X(f)$] and their fitted counterparts [$X'(f)$], the *middle row* does the same for imaginary impedance [$Y(f)$ and $Y'(f)$], and the *bottom row* for the membrane ratio [$\alpha(f)$ and $\alpha'(f)$]. The square symbols in each plot signify the measured data points, sampled at discrete frequencies [$f = \omega/(2\pi)$], while the solid lines indicate the fitted data generated using 3 P-EIS. The electronic circuit parameters (β_k) corresponding to the circuit elements in Fig. 1*C* and their corresponding fitted values using 3 P-EIS (β_k') are outlined in Table 2.

the magnitude of the real impedance (Fig. 2, *top row*) at the lowest measured frequencies represents the sum of the TER, apical, and basolateral solution resistances (R_{solA} and R_{solB}, respectively). Additionally, the real impedance at the highest measured frequencies represents the resistance of only the apical and basolateral solution resistances (R_{solA} and R_{solB}, respectively). By evaluating the real impedance [$X(\omega)$ from *Eq. 9*] at both high and low frequencies, a more accurate representation of the integrity of the epithelial tissue can be extracted by decoupling the solution and growth substrate resistances (R_{solA} and R_{solB}) from the TER.

When the cell membranes are modeled with a resistor in parallel with a capacitor as is shown in Fig. 1*C*, the imaginary impedance (Fig. 2, *middle row*), can reveal information about the time constants, τ, of the apical and basolateral membranes. In a general sense, the time constant of a cell

membrane represents how quickly it can reequilibrate after a sudden change in transmembrane voltage or current. This parameter can be calculated using the following formula:

$$\tau = RC. \quad (20)$$

One interesting feature of most epithelial tissues is that they are polarized, meaning that they have different electrical transport and functional pathways in their apical and basolateral membranes (7, 22, 58, 59). Consequently, epithelia may have distinctly different apical and basolateral time constants (32). For example, if the cells are stimulated by ATP (see MATERIALS AND METHODS), the apical and basolateral membranes of RPE typically have unique and opposite electrical responses. These unique and opposite responses of τ could be visualized as diverging or converging minimums in the imaginary impedance plot.

The membrane ratio (Fig. 2, *bottom row*) is the only property that measures the ratio of apical to basolateral impedance. At the lowest measured frequencies ($\omega \rightarrow 0$ rad/s), this system asymptotically approaches the following limit:

$$\lim_{\omega \to 0} \left(\alpha'(\omega)\right) = \frac{R_a R_s + R_{solA}(R_a + R_b + R_s)}{R_b R_s + R_{solB}(R_a + R_b + R_s)} \quad (21)$$

which simplifies to the VDR from *Eq. 1* when R_{solA} and R_{solB} are much less than the apical and basolateral resistances and can be set to ~0 (33, 34). Conversely, at high frequencies ($\omega \rightarrow \infty$ rad/s), the membrane ratio approaches the following limit:

$$\lim_{\omega \to \infty} \left(\alpha'(\omega)\right) = \frac{R_{solA}}{R_{solB}} \quad (22)$$

To demonstrate these qualitative metrics, they were applied to the representative data shown in Fig. 2 The exact values measured by the digital multimeter, β_k, for each circuit parameter k and corresponding parameter fits, β_k' are shown in Table 2. In Fig. 2, the exact TER (total epithelial resistance plus the solution resistances) for *examples 1*, *2*, and *3* were 720 Ω, 1,750 Ω, and 5,180 Ω, respectively. These correlated well with the values that can be calculated by inspecting the low-frequency asymptote of the real impedance traces shown in Fig. 2 of 720 Ω, 1,750 Ω, and 5,160 Ω, respectively. Furthermore, the exact sum of solution resistances for *examples 1*, *2*, and *3* in Fig. 2 were 198 Ω, 99 Ω, and 198 Ω, respectively. These correspond well with the high-frequency asymptotes of Fig. 2 of 210 Ω, 135 Ω, and 278 Ω, respectively.

The ratio of apical to basolateral time constants in Fig. 2 for *examples 1* and *2* are nearly identical (~25:1). Visual inspection of the imaginary impedance traces, therefore, should have two minimums. The difference in Fig. 2 in *example 2* is clear but in *example 1* appears only as a "slowing" of the return to 0 Ω for the imaginary impedance around 1 kHz. This "slowing" phenomenon shows the impact of the lower shunt resistance (R_s), attenuating the visible changes in the imaginary impedance data. Furthermore, *example 3* in Fig. 2 has a ratio of time constants 1:2,600. Notably, the second minimum is likely above the 10-kHz measurement range and is not visible in the trace. This assumption can be made by visual inspection of the imaginary impedance data because the measured data appears to be diverging away from 0 Ω at 10 kHz, hinting that another minimum may exist at higher frequencies. Despite the lack of clear visual evidence of distinct minimums in *examples 1* and *3* from Fig. 2, the calculated membrane time constants were still accurate when using the 3 P-EIS method introduced in this paper. Namely, 24:1, 26:1, and 1:620 for *examples 1*, *2*, and *3*, respectively.

Finally, visual inspection of the asymptotes of the membrane ratio (Fig. 2 bottom row) matches the limits described in *Eqs. 21* and *22*. Therefore, in Fig. 2, the low-frequency asymptotes should approach 3.9, 0.9, and 0, for *examples 1*, *2*, and *3*, respectively, which it appears to do. Similarly, the high-frequency asymptotes in the membrane ratio in Fig. 2 should be 1, 0, and 1 for *examples 1*, *2*, and *3*, respectively, which appears to be the case.

Quantification of residual error.

Figure 2 offers compelling evidence for the 3 P-EIS model's alignment with the measured data across diverse electronic circuit configurations. The residual error, as outlined in *Eq. 7*, underscores good model correlation, marked by medians and interquartile ranges (IQRs) of 1.7 Ω (1.0–4.1), 0.8 Ω (0.3–2.0), and 0.0 (0.0–0.1) ($n = 103{,}032$). The residual was low across the extensive data set comprising 972 circuits measured at 106 frequencies, resulting in a total of 103,032 data points. Additional insights into the residual distribution can be found in the Supplemental Material. These minimal residual errors substantiate the robustness and reliability of the 3 P-EIS model in accurately capturing the real impedance, imaginary impedance, and membrane ratio. Furthermore, the near-zero median residual error highlights the model's potential efficacy in discerning subtle, clinically pertinent variations in membrane properties.

Table 2. *Electronic circuit parameters and corresponding fitted parameters*

	Example 1		Example 2		Example 3	
	β	β′	β	β′	β	β′
R_{solA}, Ω	99.2	100.7	0.4	25.8	99.2	114.4
R_{solB}, Ω	98.7	100.6	98.7	77.6	98.7	0.1
R_a, Ω	988	1,186	988	946	99	150
C_a, μF	2.35	2.07	2.35	2.45	0.09	0.2
R_b, Ω	99	102	994	984	9,790	8,006
C_b, μF	1.01	1.03	0.09	0.09	2.34	2.34
R_s, Ω	1,001	869	10,029	11,436	10,029	13,072

The validated electronic circuit parameters, denoted as β, alongside their corresponding fitted parameters, denoted as β′, as obtained using 3 P-EIS. The parameters are related to the 3 representative examples illustrated in Fig. 2. Each row in the table corresponds to a specific element of the equivalent electronic circuit as depicted in Fig. 1*C*. See GLOSSARY for definitions.

Parameter estimation error for 3 P-EIS.

3P-EIS, introduced in this paper, enables the assumption-free measurement of electrical properties in epithelial tissues. To quantify this error, the relative difference between the known circuit value β_k and the calculated value β_k' was inserted into *Eq. 8* and is called parameter estimation error.

3P-EIS significantly reduces parameter estimation error compared to 2 P-EIS, which serves as a control to validate the need for intracellular data. In assessing biologically significant resistances, namely, R_a, R_b, and R_s, the data presented in Table 3 indicate an average estimation error of 24% (SD 4, $n = 3$) using 3 P-EIS. This is a substantial improvement over the 79% (SD 20, $n = 3$) error observed with 2 P-EIS. When compared with the average biological error of 51% (SD 22, $n = 27$) compiled from values reported in previous studies (Table 4), the practical utility of 3 P-EIS seems clear.

However, to disentangle the biological uncertainty from the hardware and measurement techniques an ANOVA on existing data recorded from one epithelial tissue type, using three independent techniques, can be performed. Specifically, the three different techniques deployed by Bello-Reuss to measure R_a, R_b, and R_s for *Ambystoma tigrinum* have an ANOVA P value of 0.8, and a minimum Tukey honestly significant difference post hoc test P value of 0.8 between the glucose and Ba^{2+} groups. This indicates that variations in parameter magnitudes between experiments are likely caused by typical levels of biological variability rather than measurement technique(s) and hardware.

Beyond the biologically relevant resistances, 3 P-EIS can also, simultaneously, measure solution resistances R_{solA} and R_{solB}. In Table 3, the median error is notably larger than the other circuit parameters. However, this is an artifact of calculating a normalized error on very small resistances (<0.5 Ω in 5). On an absolute error scale (i.e., not normalized by the magnitude of the known parameter, β_k), R_{solA} and R_{solB} had median and IQR error of 7 Ω (1 Ω to 9 Ω) and 8 Ω (1 Ω to 21 Ω), respectively, when fitting using 3 P-EIS. Besides this error being very small relative to the magnitude of the other resistances tested in this paper, solution resistances are typically measured before a practical electrophysiology experiment and do not provide pertinent information when trying to understand the electrophysiological properties of epithelial tissue. However, the ability to monitor these resistances throughout, as opposed to before, an experiment can be beneficial. For example, when the solution resistance changes or when the cell growth substrate degrades throughout an experiment.

Table 3. *Comparison of fitting errors between the 3 P-EIS and 2 P-EIS methods*

	3 P-EIS, %	2 P-EIS, %	*P* Value	Effect Size
C_a	11 (3–54)	52 (14–100)	1×10^{-37}	0.41
C_b	14 (3–57)	50 (14–98)	1×10^{-39}	0.42
R_a	28 (11–83)	94 (47–793)	1×10^{-38}	0.42
R_b	26 (7–75)	92 (45–530)	1×10^{-63}	0.54
R_s	19 (6–78)	51 (13–200)	2×10^{-9}	0.19
R_{solA}	100 (9–952)	96 (46–952)	4×10^{-21}	0.3
R_{solB}	100 (10–1,971)	99 (47–1,053)	9×10^{-14}	0.25

Comparison between the median and interquartile range of fitting errors between the 3 P-EIS and 2 P-EIS methods, calculated as per *Eq. 8* ($n = 972$). Statistical analysis includes a one-sided Wilcoxon's paired sample test and calculation of effect size for each parameter. The aim of the statistical comparison was to evaluate the significance and the effect size of the differences between the 2 models. Further graphical representation of these results can be found in the Supplemental Material. See GLOSSARY for definitions.

Table 4. *Comparative analysis of the average errors in measuring apical, basolateral, and shunt resistances in epithelial tissues, based on published literature*

Source	*n*	R_a, %	R_b, %	R_s, %
Bello-Reuss (44)				
Rabbit proximal tubules				
Ba^{2+}	8	77	44	83
Glucose	7	49	48	18
Ambystoma tigrinum				
Glucose	9	20	45	57
Ba^{2+}	13	53	64	52
K^+	6	49	32	38
Joseph and Miller (43)				
Retinal pigment epithelial				
Ouabain	9	38	46	24
Reuss and Finn (35)				
Toad urinary bladder				
Multiple intracellular electrodes	8	30	52	79
K^+	9	76	97	99
Wills et al. (57)				
Rabbit descending colon				
Nystatin	6	43	36	22

The errors are represented as percentages, calculated using the mean (μ) and standard error (SE) via the formula: $\text{error}\,(\%) = 100\sqrt{n}(SE)/\mu$. The "source" column specifies the authors along with the citation number, the tissue type investigated, and the measurement technique employed. Except for the "multiple intracellular electrodes" method, all techniques summarized below involve modulating the tissue electrophysiological state with a stimulus (e.g., glucose), while assuming the stimulus affects only a subset of the resistances. The resistances are then calculated using electrical properties measured in 2 or more states and a corresponding set of equations. See GLOSSARY for definitions.

Although capacitance is defined by $C = \varepsilon A/L$, where ε is a dielectric constant, A is surface area, and L is membrane thickness, it is generally assumed that ε and L are constant for cell membranes. Further, the ratio of ε/L is similar in magnitude across many cell types. As a result, the cell capacitance (C) is generally accepted to be around 1 μF/cm^2, and alterations in measured capacitance most likely indicate changes in membrane surface area (32, 52, 60, 61). To understand the typical variance in cell capacitance in physiological experiments, it is instructive to examine existing literature. For example, both Weber et al. (62) and Takahashi et al. (63) reported 3′,5′-cyclic monophosphate (cAMP)-induced increases in *Xenopus laevis* oocyte membrane capacitance, ranging from 12 to 60%. From Table 3, 3 P-EIS has a median error of 11% for C_a and 14% for C_b, with respective IQRs of 3–54% and 3–57%. Given this distribution, the system is likely sensitive enough to detect changes of the magnitudes reported by Weber et al. (62) and Takahashi et al. (63), albeit with caveats. Specifically, the skewed error distribution implies that while the system may generally be reliable, there are instances where significant errors could occur. These findings, therefore, should be interpreted cautiously, particularly when approaching the boundaries of this reported range of physiological changes.

While the 3 P-EIS model appears to have sufficient sensitivity for most biological experiments on epithelial tissues, it

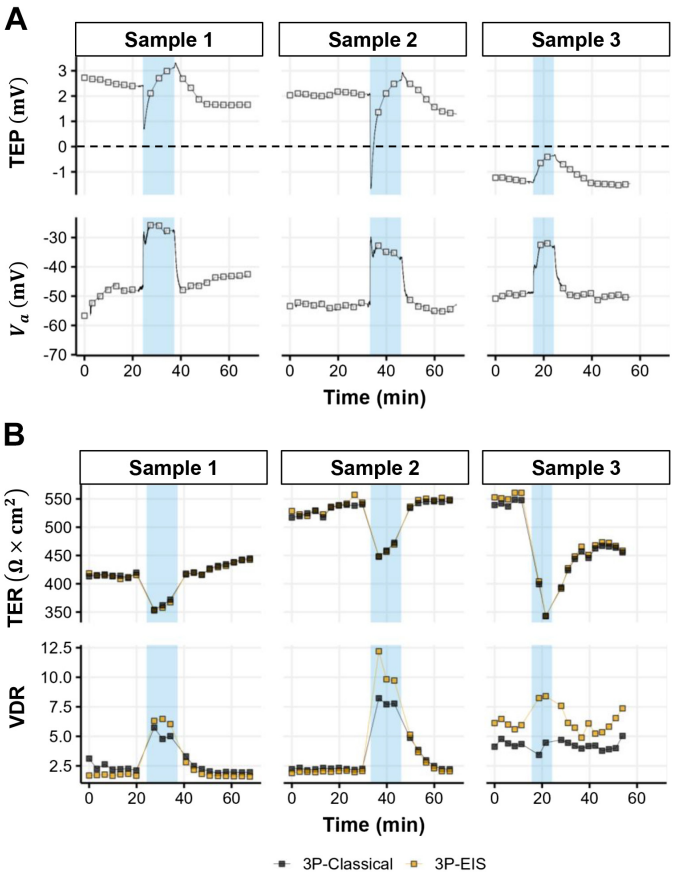

Figure 3. Electrophysiological data acquired from 3 induced pluripotent stem cell (iPSC)-derived retinal pigment epithelial (RPE) samples. Blue bars indicate the time range over which 100 μM ATP was exposed to the apical side of the RPE. *Samples 1* and *2* were from *donor A* and sample 3 was from *donor B* ($n = 3$). *A*: the transepithelial potential (TEP) (*top row*) and pipette voltage (V_a; *bottom row*) were continuously recorded between impedance measurements and their corresponding measured values are indicated with a solid black line. The square symbols highlight the magnitude of the TEP and pipette voltage immediately before starting each impedance measurement. The dashed black line indicates 0 mV to highlight the polarity of each iPSC-RPE tissue. *B*: comparison of the calculated or fitted data acquired using the 3 P-Classical technique and the value determined from the fitted parameters using the 3 P-EIS method. Specifically, the 3 P-Classical data are indicated by the black squares (connected by a black line to indicate continuity) and are calculated using the magnitudes of $TEP(f = 0.5\ \text{Hz})$ and $i_{applied}(f = 0.5\ \text{Hz})$ in *Eq. 2* for transepithelial resistance (TER) and the magnitudes of $V_a(f = 0.5\ \text{Hz})$ and $V_b(f = 0.5\ \text{Hz})$ in *Eq. 1* for voltage divider ratio (VDR). The equivalent TER and VDR values for 3 P-EIS are indicated by the orange squares (connected with an orange line to indicate continuity) where the fitted values β'_k were inserted into the right-hand side of *Eq. 2* for TER and *Eq. 1* for VDR.

is not without some shortcomings. For instance, each measurement is 2 min, and, following Nyquist's sampling theorem, cannot be used to measure dynamic processes that change within a period of less than 4 min; effectively steady state. An example of a response that is missed by 3 P-EIS is the initial phase of the ATP response in the TEP data (Fig. 3*A*). Potential solutions to this limitation include reducing the number of frequencies required per decade, decreasing the number of cycles needed to capture each frequency, or using more complex signals such as chirps that quickly sweep through a large frequency range (64).

The stability of the fitting algorithm also has its limits. In 265 out of the 927 fits, one of the membrane resistance parameters (R_a, R_b, and R_s) was estimated to be within 1% of the maximum value constrained by the fitting algorithm (termed "railing"). In contrast, the capacitances and solution resistances (C_a, C_b, R_{solA}, and R_{solB}) did not rail.

While there is not a singular cause for this railing condition, it only occurs in one of the membrane resistance parameters at a time. In other words, if R_a railed, then R_b and R_s did not, and so on. Furthermore, the impact on the estimation error for a particular railing condition was dependent on which parameter railed. For instance, when R_a railed, the parameter estimation errors were relatively unchanged. However, when R_b railed, C_a, R_a, and R_{solA} parameter estimation error increased, matching the median error for 2 P-EIS. Finally, when R_s railed, the magnitude of all other parameter estimation errors resembled that of 2 P-EIS. This increase in error suggests that the sensitivity of the remaining parameters is reduced in cases with "railing." For a detailed look at the effect of railing on the remaining circuit parameters, see the Supplemental Material.

The 3 P-EIS mathematical model and technique have demonstrated the ability to accurately determine the independent apical, basolateral, and shunt resistances and capacitances of the circuit model (Fig. 1*C*) within biologically relevant ranges with a biologically useful degree of accuracy. This highlights the value of 3 P-EIS in characterizing the electrical properties of epithelial tissues, offering new insights into biological systems and the potential for further advancements in drug discovery, channels/pathway experiments, and quality control metrics.

Demonstration on Biological Samples

To biologically validate the mathematical model presented in this paper, the response of three RPE tissues to the apical application of 100 μM ATP was measured over a one-hour period using both 3 P-Classical (measuring TER and VDR at one, low frequency) and 3 P-EIS. The ATP response of iPSC-derived RPE tissues (from 2 donors) was selected for this validation because the ATP pathway has been thoroughly tested on primary bovine, human RPE, and iPSC-derived RPE cells (7, 38, 39). In short, in the eye, light causes ATP to increase in the subretinal space, resulting in intracellular RPE Ca^{2+} signaling triggered by activated apical purinergic $P2Y_2$ receptors (38). The increase in intracellular Ca^{2+} causes the inhibition of Ca^{2+}-sensitive apical membrane K^+ channels as well as the activation of Ca^{2+}-sensitive, basolateral membrane Cl^- channels (7, 39). Inhibition of apical membrane K^+ channels reduces membrane conductance, causing the apical membrane resistance (R_a) to increase. Analogously, activation of the basolateral membrane Cl^- channels cause a decrease in the basolateral membrane resistance (R_b). Although R_a and R_b are well understood in this paradigm, the responses of C_a, C_b, and R_s are not yet well understood.

Epithelial voltages.

To begin, the TEP and apical voltage (V_a) were continuously recorded and can be used to begin the interpretation of the ATP-evoked response for both the 3 P-Classical and 3 P-EIS methods (Fig. 3*A*). Figure 3*A*, *top row*, shows the TEP data and reveals the difference in the apical and basolateral

membrane voltages (31, 55, 57, 65). *Sample 3* had an opposite TEP polarity at baseline and is missing the first phase TEP decrease (within the first minute) of the ATP-evoked response compared to *samples 1* and *2*. All three samples showed an increase in TEP over the remainder of the ATP exposure and recovered to their original values after returning to normal Ringer's solution.

Figure 3*A*, *bottom row*, shows the intracellular voltage data measured with the pipette, which corresponds to the apical membrane potential (V_a). The potential recorded by the pipette before and after apical ATP is normal (e.g., less than −45 mV) and relatively stable for *samples 1*, *2*, and *3* in the standard Ringer's solutions (7, 38, 65, 66). The depolarization of the apical membrane in the first phase of the ATP-induced response was present yet smaller for *sample 3* compared to *samples 1* and *2* (10 mV compared to 20 mV, respectively). However, all three samples depolarized by ~20 mV by the end of the ATP exposure.

Epithelial resistances.

Figure 3*B* shows the TER and VDR of the same samples in Fig. 3*A*. These parameters were calculated using two different methods: 3 P-Classical and 3 P-EIS. The TER and VDR from 3 P-Classical were determined as described in the MATERIALS AND METHODS and the TER and VDR from 3 P-EIS were calculated by inserting the estimated parameters (R_{solA}, R_{solB}, R_a, R_b, and R_s) into *Eqs. 2* and *1*, respectively.

The results presented in Fig. 3*B*, *top row*, show nearly identical TER using either the 3 P-Classical or 3 P-EIS method. Both methods depict a decrease in TER during ATP exposure and some recovery after ATP removal, consistent with previous reports (7, 38, 39). However, TER measurements alone cannot distinguish between changes in R_a, R_b, and R_s. To gain more insight, VDR was also measured (Fig. 3*B*, *bottom row*), and additional information about the relative changes in the membrane-specific resistances (R_a and R_b) can be evaluated.

In Fig. 3*B*, note the discrepancies in magnitude between the VDR obtained through the 3 P-EIS method and the 3 P-Classical method during ATP stimulation for *samples 1* and *2*, as well as across all tests for *sample 3*. The key discrepancy arises from the limitations of sampling at a single, discrete frequency (0.5 Hz) in 3 P-Classical, which sometimes fails to accurately approximate the membrane ratio's asymptote as it approaches 0 Hz. Unlike 3 P-Classical, which requires near-zero frequencies to accurately account for all capacitive effects, 3 P-EIS offers significant flexibility by allowing for data extrapolation to theoretical VDR values at 0 Hz. This extrapolation advantage enables 3 P-EIS to perform robustly in dynamic conditions requiring faster sampling rates, delivering superior VDR accuracy and even capturing dynamic changes in VDR that could be missed with 3 P-Classical (e.g., the change in VDR during apical-ATP for *sample 3*). Moreover, 3 P-EIS sidesteps the inherent unpredictability of the 3 P-Classical method, which cannot predetermine the optimal frequency for precise VDR measurements. For further details on real and imaginary impedance and membrane ratios, consult Supplemental Material.

Unique to 3 P-EIS (compared to 3 P-Classical), the solution resistances (R_{solA} and R_{solB}) were calculated using the 3 P-EIS model. The solution resistances were relatively consistent magnitude before, during, and after ATP exposure. Consequently, the average magnitude of these values was 3 (SD 3) $\Omega \times cm^2$ and 9 (SD 1) $\Omega \times cm^2$ for R_{solA} and R_{solB}, respectively ($n = 85$). The elevated R_{solB} is likely due to the extra resistance of the growth substrate. Furthermore, the magnitude of the sum of these resistances corresponds well with historical measurements of the resistances of empty growth substrates installed in the modified Ussing chamber, submerged in Ringer's control solutions, typically between 10 and 20 $\Omega \times cm^2$. The ability to monitor the solution resistance during an experiment is an important improvement over 3 P-Classical. For example, when cells are grown on biodegradable scaffolds or when cells secrete large amounts of extracellular matrix, R_{solB} may increase or decrease in a manner that is difficult to compensate for, masking subtle changes in electrical parameters between samples.

3P-EIS offers a continuous, assumption-free approach to quantifying all circuit parameters outlined in Fig. 1*C*, as demonstrated in Fig. 4. Focusing initially on apical,

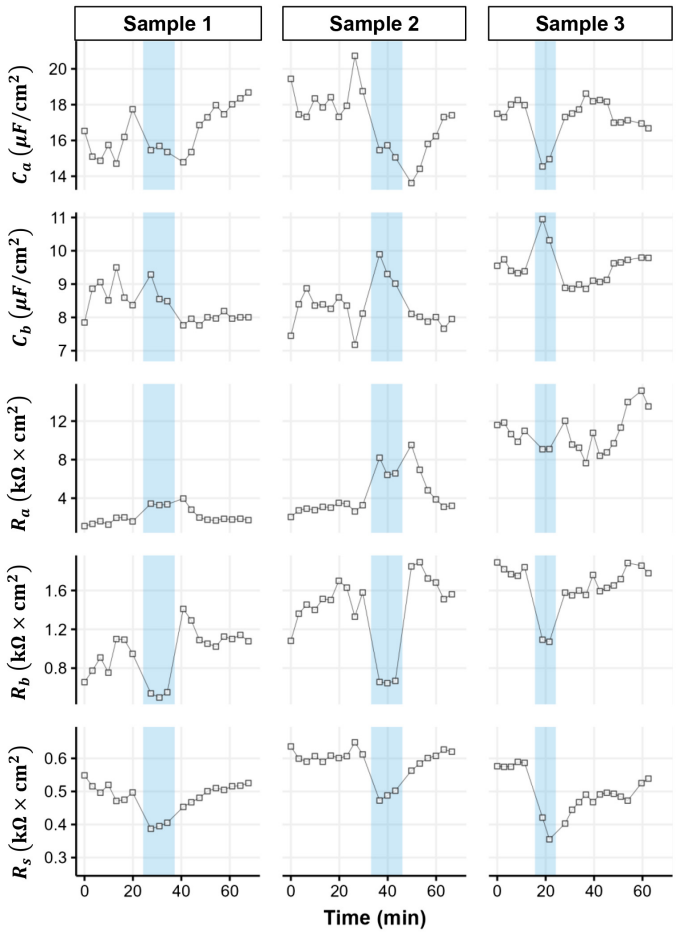

Figure 4. The capacitance and resistance responses of pluripotent stem cell (iPSC)-derived retinal pigment epithelial (RPE) samples before, during, and after the addition of 100 μM ATP to the Ringer's solution perfusing the apical membrane. The values were calculated using the 3 P-EIS method. Blue shading indicates the time that ATP was in the apical media. The white squares indicate the calculated values, and the black lines represent an interpolated values between each measurement. Each column corresponds to a unique iPSC-RPE sample. Each row corresponds to 1 of the circuit elements from Fig. 1*C* *samples 1* and *2* are from *donor A* and *sample 3* is from *donor B* ($n = 3$). See GLOSSARY for definitions.

basolateral, and shunt resistances (R_a, R_b, and R_s, respectively), *sample 3* from *donor B* exhibits a markedly elevated baseline apical resistance (R_a) of ~11 kΩ × cm^2. This contrasts with 1.6 kΩ × cm^2 and 3.3 kΩ × cm^2 for *samples 1* and *2*, respectively. One possible explanation for this observation, based on recent literature, indicates that stem cell-derived RPE lines have heterogeneous densities of K^+ channels between neighboring cells in a single epithelial tissue. This heterogeneity phenomenon can provide an explanation for the elevated R_a in *sample 3* (67). A lower number of K^+ channels on the apical membrane would correspondingly result in higher resistance and a diminished ATP response, as is observed in *sample 3*. Conversely, the basolateral resistance (R_b) remains comparable to that of *samples 1* and *2*, and it shows the expected reduction during ATP exposure, likely due to the activation of basolateral Ca^{2+}-sensitive Cl^- channels. Finally, across all samples the shunt resistance (R_s) depicts a rapid and substantial decrease during ATP exposure and has a long recovery back to baseline.

3 P-EIS proves to be especially useful when epithelial responses involve complex interactions between membranes, as is the case with typical ATP responses in RPE (7, 38, 39). Unlike 3 P-Classical, which struggles to independently measure membrane resistances, 3 P-EIS can distinguish the atypical apical membrane response from the typical basolateral membrane response, as illustrated in *sample 3*. This allows for a nuanced understanding of cellular behavior in different experimental conditions not possible with 3 P-Classical.

Epithelial capacitances.

Utilizing 3 P-EIS to calculate membrane-specific capacitances (C_a and C_b) from in Fig. 1*C*, the data consistently reveals an apical-to-basolateral capacitance ratio of ~2:1, across all samples, in control Ringer's solution, both pre- and post-ATP stimulation. This suggests that the apical surface area of RPE cells may be twice as large as the basolateral area, aligning with prior literature reports indicating a 4:1 ratio of surface areas for rat RPE (2, 61, 68).

Investigation of the membrane-specific ATP-induced capacitance changes (Fig. 4) shows a difference between *sample 1* compared to *samples 2* and *3*. *Sample 1* did not display ATP-induced changes. In contrast, *samples 2* and *3* experienced concurrent reductions in apical capacitance and elevations in basolateral capacitance during apical ATP stimulation. These changes could potentially signify a reduction in apical membrane microvilli and increased lateral intercellular spaces (corroborated by a reduction in the shunt resistance), respectively. However, it is also possible that if conformational molecular changes occur during ATP exposure, an alternative explanation for changes in the apical membrane could be modifications in membrane composition, specifically membrane thickness or dielectric constant (38, 52, 60, 69).

Limited existing literature on membrane capacitance variability, particularly during ATP stimulation in RPE, precludes any definitive conclusions. Due to the small sample size in this biological demonstration, future studies employing larger datasets are imperative for conclusive interpretations of this data.

Using 3 P-EIS to test assumption-based methods during ATP administration on RPE cells.

Data acquired using 3 P-EIS can be used to test the validity of assumptions used in alternative methods to fully solve for all membrane parameters, β_k, in Fig. 1*C*. For starters, Fig. 4 clearly shows that all membrane resistances change (R_a, R_b, and R_s) change when ATP is applied, undermining assumptions leveraged by previous groups where at least one membrane must remain constant to fully solve for these parameters (35, 43–45, 57). Another assumption leveraged to fully determine β_k used measurements from previous experiments of a particular wild-type control cell line and asserted that the ratio of transcellular to shunt resistance was constant, even during specific drug exposures (41). However, the data presented in this paper clearly shows that this ratio $[(R_a + R_b)/ R_s]$ is not constant and was dramatically different for *sample 3* compared to *samples 1* and *2* (see Supplemental Material for details).

As such, traditional approaches risk overlooking or misinterpreting meaningful variations in epithelial tissues by relying on these assumptions. 3 P-EIS is devoid of such limitations, providing a more resilient and assumption-independent approach. This enables comprehensive evaluations of how epithelial transport pathways are affected across various scenarios including drug treatments, disease conditions, and quality control measures.

Summary of Findings

This paper introduces 3 P-EIS, a method for quantifying the membrane-specific properties that make up an equivalent electrical circuit of intact epithelial tissues. This method uses a combination of an intracellular pipette and extracellular EIS to resolve the transcellular and paracellular electrical properties without constraint-based assumptions previously required to evaluate these metrics (35, 41, 43–45, 57). Specifically, 3 P-EIS measures the apical resistance R_a, apical capacitance C_a, basolateral resistance R_b, basolateral capacitance C_b, and shunt resistance R_s of intact epithelial tissues. Furthermore, 3 P-EIS can simultaneously measure the resistance of the surrounding media and culture substrate to compensate for changes throughout an experiment, further improving the accuracy of the epithelial parameters. Rigorous validation with electronic cell components quantifies the accuracy of 3 P-EIS and an examination of typical biological variability suggests that the model is suitable for use in studying epithelia.

Advancements over previous methods.

The addition of EIS in existing 3 P-Classical setups enables 3 P-EIS. Unlike 3 P-Classical and other more sophisticated approaches, 3 P-EIS allows for a nuanced understanding of epithelial physiology based on additional electrical parameters measured by this technique. These parameters previously required additional measurements or assumptions to evaluate, and 3 P-EIS unlocks a new way to enhance epithelial transport dynamics quantification.

Clinical and research implications.

For research, 3 P-EIS provides a more precise readout of epithelial physiology and enhances the details extracted when studying novel pathways diseases. It also, potentially,

provides dynamic readouts of cell morphology without a microscope or other destructive techniques. The utility of 3 P-EIS extends beyond basic research. In the clinical realm, this method offers a new avenue for drug testing where membrane-specific changes or interactions are underdetermined when using 3 P-Classical or in assumption-based methods that assume normal cell function. Furthermore, this method could be used as a higher sensitivity quality control metric in transplantation therapies.

GLOSSARY

- α Measured ratio of apical to basolateral membrane impedance magnitude
- α' Calculated ratio of apical to basolateral membrane impedance magnitude
- β Represents an arbitrary electronic circuit component (e.g., *R* or *C*)
- ε Relative error
- μ Average
- τ Electrical time constant measure in seconds.
- ω Frequency in rad/s
- C_a Electrical capacitance of the apical membrane of epithelia measured in F/cm^2
- C_b Electrical capacitance of the basolateral membrane of epithelia measured in F/cm^2
- d A single datum measured or fit at a particular measurement frequency
- J Objective function to be minimized during fitting of electronic circuit components
- r Difference (residual) between a measured and calculated value
- R_a Electrical resistance of the apical membrane of epithelia
- R_b Electrical resistance of the basolateral membrane of epithelia
- R_s Electrical resistance of the shunt pathways between and around epithelial cells
- R_{solA} Electrical resistance of apical solution
- R_{solB} Electrical resistance of basolateral solution and growth substrate
- V Electrical voltage measured in volts
- X Measured real component of complex impedance (resistance) in $\Omega \cdot cm^2$
- Y Measured imaginary component of complex impedance (reactance) in $\Omega \cdot cm^2$
- X' Calculated real component of complex impedance (resistance) in $\Omega \cdot cm^2$
- Y' Calculated imaginary component of complex impedance (reactance) in $\Omega \cdot cm^2$
- Z_{abs} Complex electrical impedance of epithelia measured in $\Omega \cdot cm^2$

DATA AVAILABILITY

Data are available at the Github repository (called "3P-EIS") https://github.com/colbyNIH/3P-EIS.

SUPPLEMENTAL MATERIAL

Supplemental Table S1: https://doi.org/10.6084/m9.figshare.24393040.

Supplemental Table S2: https://doi.org/10.6084/m9.figshare.24393337.

Supplemental Fig. S1: https://doi.org/10.6084/m9.figshare.24393628.

Supplemental Fig. S2: https://doi.org/10.6084/m9.figshare.24393760.

Supplemental Fig. S3: https://doi.org/10.6084/m9.figshare.24393946.

Supplemental Fig. S4: https://doi.org/10.6084/m9.figshare.24394222.

Supplemental Fig. S5: https://doi.org/10.6084/m9.figshare.24394504.

Supplemental Fig. S6: https://doi.org/10.6084/m9.figshare.24394621.

Supplemental Fig. S7: https://doi.org/10.6084/m9.figshare.24394711.

Supplemental Fig. S8: https://doi.org/10.6084/m9.figshare.24394795.

Supplemental Dataset: https://doi.org/10.6084/m9.figshare.24395053.

GRANTS

This work was funded by National Institutes of Health Grants RF1AG079269, R01NS102727, 1U01MH106027, and R01DA029639, National Science Foundation Graduate Research Fellowship Program, and National Eye Institute Intramural Research Program to K.B.

DISCLOSURES

No conflicts of interest, financial or otherwise, are declared by the authors.

AUTHOR CONTRIBUTIONS

C.F.L., A.M., K.B., and C.R.F. conceived and designed research; C.F.L., R.H., D.R. and R.S. performed experiments; C.F.L. analyzed data; C.F.L., A.C., A.M., Q.W., K.B., and C.R.F. interpreted results of experiments; C.F.L. prepared figures; C.F.L., A.C., K.B., and C.R.F. drafted manuscript; C.F.L., A.C., A.M., R.H., Q.W., K.B., and C.R.F. edited and revised manuscript; C.F.L., A.C., A.M., R.H., D.R., R.S., Q.W., K.B., and C.R.F. approved final version of manuscript.

REFERENCES

1. **Anderson JM**, **Itallie CM.** Physiology and function of the tight junction. *Cold Spring Harb Perspect Biol* 1: a002584, 2009. doi:10.1101/cshperspect.a002584.
2. **Rizzolo LJ**, **Peng S**, **Luo Y**, **Xiao W.** Integration of tight junctions and claudins with the barrier functions of the retinal pigment epithelium. *Prog Retin Eye Res* 30: 296–323, 2011. doi:10.1016/j.preteyeres.2011.06.002.
3. **Cereijido M**, **Robbins ES**, **Dolan WJ**, **Rotunno CA**, **Sabatini DD.** Polarized monolayers formed by epithelial cells on a permeable and translucent support. *J Cell Biol* 77: 853–880, 1978. doi:10.1083/jcb.77.3.853.
4. **Schumann M**, **Siegmund B**, **Schulzke JD**, **Fromm M.** Celiac disease: role of the epithelial barrier. *Cell Mol Gastroenterol Hepatol* 3: 150–162, 2017. doi:10.1016/j.jcmgh.2016.12.006.
5. Skach WR (Editor)**.** *Cystic Fibrosis Methods and Protocols*. Totowa, NJ: Humana, 2002.
6. **Tang SC**, **Leung JC**, **Chan LY**, **Tsang AW**, **Lai KN.** Activation of tubular epithelial cells in diabetic nephropathy and the role of the peroxisome proliferator-activated receptor-γ agonist. *J Am Soc Nephrol* 17: 1633–1643, 2006. doi:10.1681/ASN.2005101113.
7. **Miyagishima KJ**, **Wan Q**, **Corneo B**, **Sharma R**, **Lotfi MR**, **Boles NC**, **Hua F**, **Maminishkis A**, **Zhang C**, **Blenkinsop T**, **Khristov V**, **Jha BS**, **Memon OS**, **D'Souza S**, **Temple S**, **Miller SS**, **Bharti K.** In pursuit of

authenticity: induced pluripotent stem cell-derived retinal pigment epithelium for clinical applications. *Stem cells Transl Med* 5: 1562–1574, 2016. doi:10.5966/sctm.2016-0037.
8. **Choung RS**, **Unalp-Arida A**, **Ruhl CE**, **Brantner TL**, **Everhart JE**, **Murray JA.** Less hidden celiac disease but increased gluten avoidance without a diagnosis in the USA: findings from the National Health and Nutrition Examination Surveys from 2009 to 2014. *Mayo Clin Proc* 92: P30–P38, 2016. doi:10.1016/j.mayocp.2016.10.012. .
9. **Caio G**, **Volta U**, **Sapone A**, **Leffler DA**, **De Giorgio R**, **Catassi C**, **Fasano A.** Celiac disease: a comprehensive current review. *BMC Med* 17: 142, 2019. doi:10.1186/s12916-019-1380-z.
10. **Allan KM**, **Farrow N**, **Donnelley M**, **Jaffe A**, **Waters SA.** Treatment of cystic fibrosis: from gene- to cell-based therapies. *Front Pharmacol* 12: 639475, 2021. doi:10.3389/fphar.2021.639475.
11. **Reed J**, **Bain S**, **Kanamarlapudi V.** A review of current trends with type 2 diabetes epidemiology, aetiology, pathogenesis, treatments and future perspectives. *Diabetes Metab Syndr Obes* 14: 3567–3602, 2021. doi:10.2147/DMSO.S319895.
12. **Ammar MJ**, **Hsu J**, **Chiang A**, **Ho AC**, **Regillo CD.** Age-related macular degeneration therapy: a review. *Curr Opin Ophthalmol* 31: 215–221, 2020. doi:10.1097/ICU.0000000000000657.
13. **Farhadifar R**, **Röper JC**, **Aigouy B**, **Eaton S**, **Jülicher F.** The influence of cell mechanics, cell-cell interactions, and proliferation on epithelial packing. *Curr Biol* 17: 2095–2104, 2007. doi:10.1016/j.cub.2007.11.049.
14. **Jin Lee HW**, **Wark AM**, **Corn R.** Microarray methods for protein biomarker detection. *Analyst* 133: 975–983, 2008. doi:10.1039/B717527B.
15. **Lovén J**, **Orlando DA**, **Sigova AA**, **Lin CY**, **Rahl PB**, **Burge CB**, **Levens DL**, **Lee TI**, **Young RA.** Revisiting global gene expression analysis. *Cell* 151: 476–482, 2012. doi:10.1016/j.cell.2012.10.012.
16. **Hassan Q**, **Ahmadi S**, **Kerman K.** Recent advances in monitoring cell behavior using cell-based impedance spectroscopy. *Micromachines (Basel)* 11: 590, 2020. doi:10.3390/MI11060590.
17. **Dorjsuren D**, **Eastman RT**, **Song MJ**, **Yasgar A**, **Chen Y**, **Bharti K**, **Zakharov AV**, **Jadhav A**, **Ferrer M**, **Shi PY**, **Simeonov A.** A platform of assays for the discovery of anti-Zika small-molecules with activity in a 3D-bioprinted outer-blood-retina model. *PLoS One* 17: e0261821, 2022. doi:10.1371/journal.pone.0261821.
18. **Zoio P**, **Lopes-Ventura S**, **Oliva A.** Barrier-on-a-chip with a modular architecture and integrated sensors for real-time measurement of biological barrier function. *Micromachines* 12: 816, 2021. doi:10.3390/mi12070816.
19. **Vigh JP**, **Kincses A**, **Ozgür B**, **Walter FR**, **Santa-Maria AR**, **Valkai S**, **Vastag M**, **Neuhaus W**, **Brodin B**, **Dér A**, **Deli MA.** Transendothelial electrical resistance measurement across the blood–brain barrier: a critical review of methods. *Micromachines (Basel)* 12: 685, 2021. doi:10.3390/mi12060685.
20. **Raut B**, **Chen LJ**, **Hori T**, **Kaji H.** An open-source add-on EVOM® device for real-time transepithelial/endothelial electrical resistance measurements in multiple transwell samples. *Micromachines (Basel)* 12: 282, 2021. doi:10.3390/mi12030282.
21. **Rajabzadeh M**, **Ungethum J**, **Herkle A**, **Schilpp C**, **Becker J**, **Fauler M**, **Wittekindt O**, **Frick M**, **Ortmanns M.** A PCB-based 24-Ch. MEA-EIS allowing fast measurement of TEER. *IEEE Sensors J* 21: 13048–13059, 2021. doi:10.1109/JSEN.2021.3067823.
22. **Schaub NJ**, **Hotaling NA**, **Manescu P**, **Padi S**, **Wan Q**, **Sharma R**, **George A**, **Chalfoun J**, **Simon M**, **Ouladi M**, **Simon CG**, **Bajcsy P**, **Bharti K.** Deep learning predicts function of live retinal pigment epithelium from quantitative microscopy. *J Clin Invest* 130: 1010–1023, 2020. doi:10.1172/JCI131187.
23. **Linz G**, **Djeljadini S**, **Steinbeck L**, **Köse G**, **Kiessling F**, **Wessling M.** Cell barrier characterization in transwell inserts by electrical impedance spectroscopy. *Biosens Bioelectron* 165: 112345, 2020. doi:10.1016/j.bios.2020.112345.
24. **Zhao PY**, **Gan G**, **Peng S**, **Wang SB**, **Chen B**, **Adelman RA**, **Rizzolo LJ.** TRP channels localize to subdomains of the apical plasma membrane in human fetal retinal pigment epithelium. *Invest Ophthalmol Vis Sci* 56: 1916–1923, 2015. doi:10.1167/iovs.14-15738.
25. **Srinivasan B**, **Kolli AR**, **Esch MB**, **Abaci HE**, **Shuler ML**, **Hickman JJ.** TEER measurement techniques for in vitro barrier model systems. *J Lab Autom* 20: 107–126, 2015. doi:10.1177/2211068214561025.
26. **Schmid T**, **Bogdan M**, **Günzel D.** Discerning apical and basolateral properties of HT-29/B6 and IPEC-J2 cell layers by impedance spectroscopy, mathematical modeling and machine Learning. *PLoS ONE* 8: e62913-12, 2013. doi:10.1371/journal.pone.0062913.
27. **Onnela N**, **Savolainen V**, **Juuti-Uusitalo K**, **Vaajasaari H**, **Skottman H**, **Hyttinen J.** Electric impedance of human embryonic stem cell-derived retinal pigment epithelium. *Med Biol Eng Comput* 50: 107–116, 2012. doi:10.1007/s11517-011-0850-z.
28. **Gondzik V**, **Awayda MS.** Methods for stable recording of short-circuit current in a Na^+-transporting epithelium. *Am J Physiol Cell Physiol* 301: C162–C170, 2011. doi:10.1152/ajpcell.00459.2010.
29. **Sheller RA**, **Cuevas ME**, **Todd MC.** Comparison of transepithelial resistance measurement techniques: chopsticks vs. endohm. *Biol Proced Online* 19: 4, 2017. doi:10.1186/s12575-017-0053-6.
30. **Frömter E.** The route of passive ion movement through the epithelium of Necturus gallbladder. *J Membr Biol* 8: 259–301, 1972. doi:10.1007/BF01868106.
31. **Miller SS**, **Steinberg RH.** Passive ionic properties of frog retinal pigment epithelium. *J Membr Biol* 36: 337–372, 1977. doi:10.1007/BF01868158.
32. **Schifferdecker E**, **Frömter E.** The AC impedance of necturus gallbladder epithelium. *Pflugers Arch* 377: 125–133, 1978. doi:10.1007/BF00582842.
33. **Yeste J**, **Illa X**, **Alvarez M**, **Villa R.** Engineering and monitoring cellular barrier models. *J Biol Eng* 12: 18, 2018. doi:10.1186/s13036-018-0108-5.
34. **Fromm M**, **Schulzke JD**, **Hegel U.** Epithelial and subepithelial contributions to transmural electrical resistance of intact rat jejunum, in vitro. *Pflugers Arch* 405: 400–402, 1985. doi:10.1007/BF00595695.
35. **Reuss L**, **Finn AL.** Passive electrical properties of toad urinary bladder epithelium: Intercellular electrical coupling and transepithelial cellular and shunt conductances. *J Gen Physiol* 64: 1–25, 1974. doi:10.1085/jgp.64.1.1.
36. **Kottra G**, **Frömter E.** Rapid determination of intraepithelial resistance barriers by alternating current spectroscopy. II. Test of model circuits and quantification of results. *Pflugers Arch* 402: 421–432, 1984. doi:10.1007/bf00583943.
37. **Clausen C**, **Lewis SA**, **Diamond JM.** Impedance analysis of a tight epithelium using a distributed resistance model. *Biophys J* 26: 291–317, 1979. doi:10.1016/S0006-3495(79)85250-9.
38. **Maminishkis A**, **Jalickee S**, **Blaug SA**, **Rymer J**, **Yerxa BR**, **Peterson WM**, **Miller SS.** The P2Y2 receptor agonist INS37217 stimulates RPE fluid transport in vitro and retinal reattachment in rat. *Invest Ophthalmol Vis Sci* 43: 3555–3566, 2002.
39. **Peterson WM**, **Meggyesy C**, **Yu K**, **Miller SS.** Extracellular ATP activates calcium signaling, ion, and fluid transport in retinal pigment epithelium. *J Neurosci* 17: 2324–2337, 1997. doi:10.1523/JNEUROSCI.17-07-02324.1997.
40. **Bialek S**, **Miller SS.** K^+ and Cl^- transport mechanisms in bovine pigment epithelium that could modulate subretinal space volume and composition. *J Physiol* 475: 401–417, 1994. doi:10.1113/jphysiol.1994.sp020081.
41. **Cottrill KA**, **Peterson RJ**, **Lewallen CF**, **Koval M**, **Bridges RJ**, **McCarty NA.** Sphingomyelinase decreases transepithelial anion secretion in airway epithelial cells in part by inhibiting CFTR-mediated apical conductance. *Physiol Rep* 9: e14928–17, 2021. doi:10.14814/phy2.14928.
42. **Awayda MS**, **Driessche WV**, **Helman SI.** Frequency-dependent capacitance of the apical membrane of frog skin: Dielectric relaxation processes. *Biophys J* 76: 219–232, 1999. doi:10.1016/S0006-3495(99)77191-2.
43. **Joseph DP**, **Miller SS.** Apical and basal membrane ion transport mechanisms in bovine retinal pigment epithelium. *J Physiol* 435: 439–463, 1991. doi:10.1113/jphysiol.1991.sp018518.
44. **Bello-Reuss E.** Cell membranes and paracellular resistances in isolated renal proximal tubules from rabbit and Ambystoma. *J Physiol* 370: 25–38, 1986. doi:10.1113/jphysiol.1986.sp015920.
45. **Krug SM**, **Fromm M**, **Günzel D.** Two-path impedance spectroscopy for measuring paracellular and transcellular epithelial resistance. *Biophys J* 97: 2202–2211, 2009. doi:10.1016/j.bpj.2009.08.003.
46. **Lewallen CF**, **Wan Q**, **Maminishkis A**, **Stoy W**, **Kolb I**, **Hotaling N**, **Bharti K**, **Forest CR.** High-yield, automated intracellular electrophysiology in retinal pigment epithelia. *J Neurosci Methods* 328: 108442, 2019. doi:10.1016/j.jneumeth.2019.108442.
47. **Kodandaramaiah SB**, **Franzesi GT**, **Chow BY**, **Boyden ES**, **Forest CR.** Automated whole-cell patch-clamp electrophysiology of

neurons in vivo. *Nat Methods* 9: 585–587, 2012. doi:10.1038/nmeth.1993.

48. **Kolb I**, **Landry CR**, **Yip MC**, **Lewallen CF**, **Stoy WA**, **Lee J**, **Felouzis A**, **Yang B**, **Boyden ES**, **Rozell CJ**, **Forest CR.** PatcherBot: a single-cell electrophysiology robot for adherent cells and brain slices. *J Neural Eng* 16: 046003, 2019. doi:10.1088/1741-2552/ab1834.
49. **Stoy WA**, **Kolb I**, **Holst GL**, **Liew Y**, **Pala A**, **Yang B**, **Boyden ES**, **Stanley GB**, **Forest CR.** Robotic navigation to subcortical neural tissue for intracellular electrophysiology in vivo. *J Neurophysiol* 118: 1141–1150, 2017. doi:10.1152/jn.00117.2017.
50. **Holst G**, **Stoy WA**, **Yang B**, **Kolb I**, **Kodandaramaiah SB**, **Li L**, **Knoblich U**, **Zeng H**, **Haider B**, **Boyden ES**, **Forest CR.** Autonomous patch clamp robot for functional characterization of neurons in vivo: development and application to mouse visual cortex. *J Neurophysiol* 121: 2341–2357, 2019. doi:10.1152/jn.00738.2018. .
51. **Kottra G**, **Haase W**, **Fromter E.** Tight-junction tightness of Necturus gall bladder epithelium is not regulated by cAMP or intracellular Ca^{2+}. II. Impedance measurements. *Pflugers Arch* 425: 535–545, 1993. doi:10.1007/BF00374881.
52. **Ohki S.** The electrical capacitance of phospholipid membranes. *Biophys J* 9: 1195–1205, 1969. doi:10.1016/S0006-3495(69)86445-3.
53. **Gallemore RP**, **Hernandez E**, **Tayyanipour R**, **Fujii S**, **Steinberg RH.** Basolateral membrane Cl^- and K^+ conductances of the dark-adapted chick retinal pigment epithelium. *J Neurophysiol* 70: 1656–1668, 1993. doi:10.1152/jn.1993.70.4.1656.
54. **Sharma R**, **Bose D**, **Montford J**, **Ortolan D**, **Bharti K.** Triphasic developmentally guided protocol to generate retinal pigment epithelium from induced pluripotent stem cells. *STAR Protoc* 3: 101582, 2022. doi:10.1016/j.xpro.2022.101582.
55. **Miller SS**, **Edelman JL.** Active ion transport pathways in the bovine retinal pigment epithelium. *J Physiol* 424: 283–300, 1990. doi:10.1113/jphysiol.1990.sp018067.
56. **Lin H**, **Kenyon E**, **Miller SS.** Na-dependent pHi regulatory mechanisms in native human retinal pigment epithelium. *Invest Ophthalmol Vis Sci* 33: 3528–3538, 1992.
57. **Wills NK**, **Lewis SA**, **Eaton DC.** Active and passive properties of rabbit descending colon: a microelectrode and nystatin study. *J Membr Biol* 45: 81–108, 1979. doi:10.1007/BF01869296.
58. **Tran V**, **Zhang X**, **Cao L**, **Li H**, **Lee B**, **So M**, **Sun Y**, **Chen W**, **Zhao M.** Synchronization modulation increases transepithelial potentials in MDCK monolayers through Na/K pumps. *PLoS One* 8: e61509, 2013. doi:10.1371/journal.pone.0061509.
59. **Blaug S**, **Rymer J**, **Jalickee S**, **Miller SS.** P2 purinoceptors regulate calcium-activated chloride and fluid transport in 31EG4 mammary epithelia. *Am J Physiol Cell Physiol* 284: C897–C909, 2003. doi:10.1152/ajpcell.00238.2002.
60. **Bakhtiari S**, **Manshadi MK**, **Candas M**, **Beskok A.** Changes in electrical capacitance of cell membrane reflect drug partitioning-induced alterations in lipid bilayer. *Micromachines (Basel)* 14: 316, 2023. doi:10.3390/mi14020316.
61. **Günzel D**, **Zakrzewski SS**, **Schmid T**, **Pangalos M**, **Wiedenhoeft J**, **Blasse C**, **Ozboda C**, **Krug SM.** From TER to trans- and paracellular resistance: lessons from impedance spectroscopy. *Ann N Y Acad Sci* 1257: 142–151, 2012. doi:10.1111/j.1749-6632.2012.06540.x.
62. **Weber WM**, **Cuppens H**, **Cassiman JJ**, **Clauss W**, **Van Driessche W.** Capacitance measurements reveal different pathways for the activation of CFTR. *Pflugers Arch* 438: 561–569, 1999. doi:10.1007/s004249900086.
63. **Takahashi A**, **Watkins SC**, **Howard M**, **Frizzell RA.** CFTR-dependent membrane insertion is linked to stimulation of the CFTR chloride conductance. *Am J Physiol Cell Physiol* 271: C1887–C1894, 1996. doi:10.1152/ajpcell.1996.271.6.C1887.
64. **Suresh R**, **Swaminathan S**, **Rengaswamy R.** Rapid impedance spectroscopy using dual phase shifted chirp signals for electrochemical applications. *Int J Hydrogen Energy* 45: 10536–10548, 2020. doi:10.1016/j.ijhydene.2019.10.031.
65. **Quinn RH**, **Miller SS.** Ion transport mechanisms in native human retinal pigment epithelium. *Invest Ophthalmol Vis Sci* 33: 3513–3527, 1992.
66. **Maminishkis A**, **Chen S**, **Jalickee S**, **Banzon T**, **Shi G**, **Wang FE**, **Ehalt T**, **Hammer JA**, **Miller SS.** Confluent monolayers of cultured human fetal retinal pigment epithelium exhibit morphology and physiology of native tissue. *Invest Ophthalmol Vis Sci* 47: 3612–3624, 2006. doi:10.1167/iovs.05-1622.
67. **Korkka I**, **Skottman H**, **Nymark S.** Heterogeneity of potassium channels in human embryonic stem cell-derived retinal pigment epithelium. *Stem Cells Transl Med* 11: 753–766, 2022. doi:10.1093/stcltm/szac029.
68. **Okami T**, **Yamamoto A**, **Omori K**, **Takada T**, **Uyama M**, **Tashiro Y.** Immunocytochemical localization of Na^+,K(+)-ATPase in rat retinal pigment epithelial cells. *J Histochem Cytochem* 38: 1267–1275, 1990. doi:10.1177/38.9.2167328.
69. **Erb L**, **Weisman GA.** Coupling of P2Y receptors to G proteins and other signaling pathways. *Wiley Interdiscip Rev Membr Transp Signal* 1: 789–803, 2012. doi:10.1002/wmts.62.